https://dx.doi.org/10.1016/j.cma.2018.04.049

Superelasticity and Wrinkles Controlled by Twisting Circular Graphene

J.W. Yan [a,b,§] and **S.K. Lai** [c,d,*,§]

[a] *Key Laboratory of Product Packaging and Logistics of Guangdong Higher Education Institutes, Jinan University, Zhuhai, Guangdong, P.R. China*

[b] *State Key Laboratory for Strength and Vibration of Mechanical Structures, Xi'an Jiaotong University, Xi'an 710049, Shanxi, P.R. China*

[c] *Department of Civil and Environmental Engineering, The Hong Kong Polytechnic University, Hung Hom, Kowloon, Hong Kong, P.R. China*

[d] *The Hong Kong Polytechnic University Shenzhen Research Institute, Shenzhen, P.R. China*

Abstract

Controllable wrinkles in terms of amplitude, wavenumber and onset torsional angle are realized by using a twisting way of circular graphene sheets. A parametric study is carried out to investigate several factors, i.e., graphene size (inner radius r_I and outer radius R_o) and torsional angle, on the wrinkle formation of graphene. The effects of both wavenumber and amplitude are investigated in detail, because they are the most critical parameters in tuning the surface morphology that is finally reflected on the electrical properties of graphene. It is found that the onset torsional angle on the formation of wrinkles decreases as the graphene size increases. When the torsional angle increases continuously, the amplitude will abruptly jump due to a sudden change in the wrinkle pattern. The wrinkle wavenumber of graphene can also be controlled by changing the ratio of the inner and outer radii (i.e., r_I/R_o). The variation of the strain energy shows that the structural transformation is reversible, this is mainly caused by the superelastic property of graphene. Hence, the formation of recyclable wrinkles can be realized by loading and unloading processes.

*Corresponding author. Tel.: (852) 2766 6060; Fax: (852) 2334 6389. *E-mail address:* sk.lai@polyu.edu.hk

§Both authors contribute equally to this paper.

Keywords: Atomistic-continuum method, surface morphology, controllable wrinkles, graphene

1. Introduction

The great discovery of a monatomic-thick two-dimensional (2D) planar graphene in the last decade has attracted tremendous attention in various engineering disciplines [1, 2]. Graphene is a 2D repetitive hexagonal honeycomb lattice structure that possesses remarkable electrical and mechanical properties. Mechanically, the Young's modulus and tensile strength of graphene are at a level of approximately 1 TPa and 100 GPa [3], respectively. Because of its unique electrical properties, it is strongly enable graphene as the most ideal material of silicon [4]. As graphene is known as a zero bandgap semiconductor, graphene transistors cannot be switched off and are not suitable for complex logic applications accordingly. Experimental studies showed that it is possible to modify the band structure by applying strains to graphene materials [4]. In reality, the free state of graphene is not perfectly planar [5, 6] in accordance with both theoretical and experimental studies. It would generate intrinsic ripples under external field stimuli due to its bending rigidity [7]. The bending properties are crucial to the morphologic manipulation of graphene under external field stimuli [6, 8]. Extending from several nm and up to 1 μm, the influence of out-of-plane deformation of graphene sheets can provide internal stress to neutralize external field stimuli. It also enables the structure of suspended sheets to remain stable with strong influence on electrical properties.

In general, ripples generated spontaneously due to thermal fluctuations are randomly distributed [6], while artificially controllable patterns are required to manufacture devices. According to the characteristics of the negative thermal

expansion coefficient, Bao et al. [9] experimentally observed the occurrence of periodic ripples in suspended graphene membranes by applying both spontaneously and thermally generated strains. The effects of the ripple orientation, wavelength and amplitude can be regulated by controlling the boundary conditions. The interaction between graphene and its substrate has a strong effect on the lattice structure, periodically rippled graphene monolayers have been commonly observed on Ru [10] and SiC surfaces [11]. Li et al. [12] further observed periodic ripples with the amplitude of several nanometers appeared at the edges of graphene by cyclic heating and cooling. Atomic scale periodic ripples have also been observed on highly ordered pyrolytic graphite by grain boundaries using a scanning tunneling microscopy [13].

In addition, Duan and his associates [14] made use of molecular dynamics simulations and continuum models to study the explicit relationship for the wavelength and amplitude of wrinkled rectangular graphene sheets. They reported that the wrinkle wavelength decreases as the shear load increases, while the amplitude firstly increases and then remains stable. Recently, Li et al. [15] used melamine foams as a sacrificial skeleton to successfully fabricate an arbitrary-shaped graphene aerogel. This graphene aerogel is superelastic in nature and it can exhibit stable and sensitive current responses, which can be used in multi-functional pressure/strain sensors such as wearable devices. Besides, the superelastic property also enables graphene to be a promising reinforced composite material. Shen and Xiang [16] investigated the nonlinear postbuckling behaviour of axially compressive graphene-reinforced composite laminated cylindrical shells in thermal environments. Although many

experimental efforts have been conducted to manipulate the wrinkle amplitude and wavelength of graphene, it should be pointed out that experimental tools can only provide coarse results since it is extremely difficult to accurately conduct and control experiments when the size of specimen entries at nanometer scales. The fabrication process of graphene is complicated and many new complex problems are emerging out unceasingly in experimental operations. In addition, experimental studies can generally provide visual and regular results to some extent, but it is still difficult to draw a universal conclusion.

In addition to experimental studies, numerous research efforts have also been contributed to explore substantial theoretical basis and methodologies. It aims to capture the inherent mechanism for the morphology control of graphene and to accurately trace its morphological evolution. Atomic simulation that is a kind of accurate method has been widely used in nanoscience fields. Although these atomic-based methods can accurately trace the atomic spatial coordinates and capture the underlying behaviour of atomic systems, they are highly expensive in terms of computational resources. Hence, a high performance computational method is greatly desired to predict the mechanical behaviour of graphene.

In this paper, a recently developed atomistic-continuum multiscale approach [26] based on the higher-order gradient theory is applied to the investigation of controllable wrinkles spontaneously generated on circular graphene sheets under various torsional effects. The higher-order Cauchy-Born rule is used to provide an exquisite linkage between the deformation of covalent bond vectors and the

macroscopical deformation gradients. The selected representative cells in this approach can reflect the lattice structure. As the atomic interaction of graphene is included in the constitutive model, the constitutive relationship of graphene can be updated at each iterative step. Therefore, this method can exactly capture the material nonlinearity of graphene for atomistic simulation but it is much time-saving. Furthermore, the contribution of the second-order gradient to the stiffness matrix is considered by the higher-order gradient theory, the geometric nonlinearity can also be reflected. The deformed pattern of monolayer graphene sheets as well as the amplitude and wavenumber of wrinkles can be characterized, this is crucial for the design of electrical elements and nano-devices. The evolution and growth of wrinkles in circular graphene sheets are also presented.

2. Atomistic-continuum approach

2.1. Higher-order gradient theory

As depicted in Fig. 1, three geometrical parameters λ_1, λ_2 and θ are introduced to map the initial equilibrium graphene transformed from a 2D planar reference configuration. These parameters denote the uniform longitudinal stretch, transverse stretch and shear strain, respectively. A representative cell, i.e., the branch-like structure in Fig. 1, is selected for analysis. The center atom is covalently surrounded by three neighboring atoms with an angle of 120º. This mapping process of the initial equilibrium graphene from the reference configuration in Fig. 1 can be expressed by

$$\begin{cases} x_1 = \lambda_1 X_1 \\ x_2 = \lambda_1 X_1 \sin\theta + \lambda_2 X_2 \\ x_3 = 0 \end{cases} \tag{1}$$

where $\mathbf{x}=\mathbf{x}(x_1, x_2, x_3)$ and $\mathbf{X} = \mathbf{X}(X_1, X_2)$ are nodal coordinates in the initial equilibrium and reference configurations, respectively.

The Cauchy-Born rule has been widely adopted as a multi-scale agent to offer a fundamental linkage between the deformation of lattice vectors and the deformation gradients in a continuum field. However, the standard Cauchy-Born rule cannot be directly applied to the investigation of one-atom ultrathin materials. The previous computational results [17] showed a zero bending stiffness based on the standard Cauchy-Born rule. Later, Guo et al. [18] and Wang et al. [19] employed a higher-order Cauchy-Born rule to modify the bending stiffness of single-walled carbon nanotubes (SWCNTs). Based on the standard and higher-order Cauchy-Born rules, Sun and Liew [20, 21] developed a mesh-free computational framework to simulate the buckling behaviour of single-walled carbon nanotubes under axial compression and torsion. The results showed that the higher-order Cauchy-Born rule can accurately capture the bending stiffness of SWCNTs rather than the standard one.

In fact, the involved second deformation gradients in the higher-order Cauchy-Born rule can exactly describe the bending stiffness, so that the modified constitutive model is much more reasonable. Since the hexagonal lattice of graphene is a Bravais multi-lattice, it is not centrosymmetric in nature and an inner shift vector $\boldsymbol{\eta}$ is required to maintain the minimum potential of a system. The deformed bond vector $\mathbf{r}_{IJ}$ between the atoms *I* and *J* can be calculated by

$$\mathbf{r}_{IJ} = \mathbf{F}\cdot(\mathbf{R}_{IJ}+\boldsymbol{\eta}) + \frac{1}{2}\mathbf{G}:[(\mathbf{R}_{IJ}+\boldsymbol{\eta})\otimes(\mathbf{R}_{IJ}+\boldsymbol{\eta})] \tag{2}$$

where $\mathbf{F}=\dfrac{\partial \mathbf{x}}{\partial \mathbf{X}}$ and $\mathbf{G}=\dfrac{\partial^2 \mathbf{x}}{\partial \mathbf{X}^2}$ are, respectively, the first-order and second-order deformation gradient tensors from a viewpoint of the continuum displacement field that can be determined by Eq. (1). Both **r** and **R** are the C-C bond vectors in the current and reference configurations, respectively (Fig. 1).

The Tersoff-Brenner potential as the widely used empirical potential has been successfully employed to reflect the atomic interactions [22, 23]. For carbon-based nanomaterials, there are two sets of parameters and the second set of parameters is here employed. The energy per atom is the summation of the bond energy, which is only a function of the bond length connected to other atoms. Using Eq. (2), the energy W_{I} of the atom *I* can be expressed as

$$W_{\mathrm{I}}(\mathbf{F},\mathbf{G},\boldsymbol{\eta}) = \frac{1}{2}\sum_{\mathrm{J}=1}^{3} V_{\mathrm{IJ}}(\mathbf{r}_{\mathrm{I2}},\mathbf{r}_{\mathrm{I2}},\mathbf{r}_{\mathrm{I3}}) = V_{\mathrm{I}}[\mathbf{F},\mathbf{G},\boldsymbol{\eta}] \tag{3}$$

For a given deformation description, the inner shift $\boldsymbol{\eta}$ can be determined by

$$\frac{\partial V_{\mathrm{I}}}{\partial \boldsymbol{\eta}} = \mathbf{0} \tag{4}$$

in which the strain energy only depends on the first-order and second-order deformation gradients **F** and **G**.

Define the area strain energy density as

$$\omega_{\mathrm{I}}(\mathbf{F},\mathbf{G}) = \frac{W_{\mathrm{I}}[\mathbf{F},\mathbf{G},\boldsymbol{\eta}(\mathbf{F},\mathbf{G})]}{\Omega_{\mathrm{I}}}, \quad v_{\mathrm{I}} = \frac{V_{\mathrm{I}}[\mathbf{F},\mathbf{G},\boldsymbol{\eta}(\mathbf{F},\mathbf{G})]}{\Omega_{\mathrm{I}}} \tag{5}$$

with Ω_{I} being the average area per atom. The combination of the first-order and second-order deformation gradients is expressed as $\mathbf{grad} = [\mathbf{F} \quad \mathbf{G}]$. Based on Eq. (4),

the stress tensor $\boldsymbol{\sigma}$ and the tangential moduli matrix $\mathbf{M}$ can be derived as follows [24, 25]

$$\boldsymbol{\sigma} = \frac{\partial \omega_{\mathrm{I}}}{\partial \mathbf{grad}} = \frac{\partial v_{\mathrm{I}}(\mathbf{F},\mathbf{G},\boldsymbol{\eta}(\mathbf{F},\mathbf{G}))}{\partial \mathbf{grad}} = \frac{\partial v_{\mathrm{I}}}{\partial \mathbf{grad}} + \frac{\partial v_{\mathrm{I}}}{\partial \boldsymbol{\eta}} \frac{\partial \boldsymbol{\eta}}{\partial \mathbf{grad}} = \frac{\partial v_{\mathrm{I}}}{\partial \mathbf{grad}} \tag{6}$$

$$\mathbf{M} = \frac{\partial^2 \omega_{\mathrm{I}}}{\partial \mathbf{grad} \otimes \partial \mathbf{grad}} = \frac{\partial}{\partial \mathbf{grad}} \left(\frac{\partial \omega_{\mathrm{I}}}{\partial \mathbf{grad}} \right) = \frac{\partial^2 v_{\mathrm{I}}}{\partial \mathbf{grad} \otimes \partial \mathbf{grad}} + \frac{\partial^2 v_{\mathrm{I}}}{\partial \mathbf{grad} \otimes \partial \boldsymbol{\eta}} \frac{\partial \boldsymbol{\eta}_{\mathrm{I}}}{\partial \mathbf{grad}} \tag{7}$$

The first-order and second-order deformation gradients are only functions of the geometrical parameters λ_1, λ_2 and θ, so that Eq. (3) can be further rewritten as

$$v_{\mathrm{I}}[\mathbf{F},\mathbf{G},\boldsymbol{\eta}] = v_{\mathrm{I}}(\lambda_1,\lambda_2,\theta,\eta_1,\eta_2) \tag{8}$$

Denote $\boldsymbol{\lambda} = \boldsymbol{\lambda}(\lambda_1,\lambda_2,\theta,\eta_1,\eta_2)$, then it can be finally determined by the minimum potential of a representative cell

$$\frac{\partial v_{\mathrm{I}}}{\partial \boldsymbol{\lambda}} = \mathbf{0} \tag{9}$$

The Newton-Raphson method is then applied to iteratively solve Eq. (9). The real C-C bond length and the initial equilibrium configuration can be finally determined by the solved geometrical parameters. In the present simulation, the initial C-C bond length is semi-analytically evaluated to be 0.14507 nm [26].

2.2. Moving Kriging interpolation

The required C^1-continuity of the displacement interpolation, according to the involved second-order gradient in the higher-order constitutive model, yields a severe challenge when using conventional finite element methods as a discrete numerical method. Mesh-free methods have natural advantages in treating this issue. In this work, a mesh-free computational framework based on the moving Kriging (MK) interpolation [27, 29, 30] is used to numerically simulate the torsional behaviour of

circular graphene sheets.

The Kriging technique can be traced back to the first application in geo-statistics for spatial interpolation. In addition, the MK interpolation, in which the nodal information only depends on its neighboring domain, extends the Kriging interpolation to any sub-domain $\Omega(x_i)$. The sub-domain can be described by a series of dispersive nodes x_i ($i = 1, 2, \cdots, n$). Therefore, the approximate field function $\hat{u}(x)$ can be interpolated by a weighted linear combination of the given n field values as follows

$$\hat{u}(x) = \sum_{i=1}^{n} \lambda_i(x) u(x_i) \tag{10}$$

where $\lambda_i(x)$ is the weighted function of the i^{th} node. It can be determined by two factors, i.e., unbiasedness and minimum variance.

(i) **Unbiasedness**: the expected values of the approximate function $\hat{u}(x)$ must be equal to that of the given nodal values $u(x)$ as follows:

$$E\left[u(x)\right] = E\left[\hat{u}(x)\right] \tag{11}$$

(ii) **Minimum variance**: a minimum estimation error in the mean square sense is equal to:

$$\Pi = E[(u(x) - \hat{u}(x))^2] \tag{12}$$

A polynomial drift model $p_l(x)$ is expressed as

$$\sum_{i=1}^{n} \lambda_i(x) p_l(x_i) = p_l(x), \quad 1 \le l \le m, \quad p_1(x) = 1 \tag{13}$$

A commonly used linear basis in a two-dimensional space is given here as

$$\mathbf{p}^T(\mathbf{x}) = (1, x_1, x_2), \quad m = 3 \tag{14}$$

and a quadratic basis is

$$\mathbf{p}^T(\mathbf{x}) = (1, x_1, x_2, x_1^2, x_1x_2, x_2^2), \quad m = 6 \tag{15}$$

Making use of Eq. (13) as a constraint and applying a Lagrange multiplier μ_l, then Eq. (12) is rewritten as

$$\begin{aligned} \prod &= E[(u(x) - \hat{u}(x))^2] + 2\sum_{l=1}^{m} \mu_l [\sum_{i=1}^{n} \lambda_i p_l(x_i) - p_l(x)] \\ &= \sum_{i=1}^{n}\sum_{j=1}^{n} \lambda_i \lambda_j Cov(u(x_i) - u(x), u(x_j) - u(x)) + 2\sum_{l=1}^{m} \mu_l [\sum_{i=1}^{n} \lambda_i p_l(x_i) - p_l(x)] \end{aligned} \tag{16}$$

Using a semivariogram model $\gamma(h)$ to substitute the covariance $E[u(x)u(x_i)]$ yields

$$\gamma(h) = \gamma(x, x_i) = E[u(x)u(x_i)] = \frac{1}{2} E\left[\{u(x) - u(x_i)\}^2\right] \tag{17}$$

The Gaussian model [27, 28] as one of the simply used semivariogram models is selected in the present numerical simulation as a correlation function

$$\gamma(x, x_i) = \gamma(h) = 2(1 - e^{-\theta(\frac{h}{a_0})^2}) \quad (h \le a_0) \tag{18}$$

where $h = \|\mathbf{x} - \mathbf{x}_i\|$ is the vectorial distance between the nodes $\mathbf{x}$ and $\mathbf{x}_i$, and θ is an unknown correlation parameter. By fitting a sine function, the value of θ is determined to be 1 with a high conformity. a_0 is the range of a compact support domain and a circular compact support domain with a radius $r = a_0$ is chosen here. Likewise, the Gaussian models $\gamma(x, x_j)$ and $\gamma(x_i, x_j)$ are also adopted to evaluate $E[u(x)u(x_j)]$ and $E[u(x_i)u(x_j)]$, respectively,

$$2\gamma(x_i, x_j) = E\left[u(x_i) - u(x_j)\right]^2 = 2\gamma(x, x_i) + 2\gamma(x, x_j) - 2\,\mathrm{cov}\left[u(x_i) - u(x), u(x_j) - u(x)\right] \tag{19}$$

Then, Eq. (19) can be rewritten as

$$Cov(u(x) - u(x_j), u(x_i) - u(x_j)) = \gamma(x, x_j) + \gamma(x_i, x_j) - \gamma(x, x_i) \tag{20}$$

Substituting Eq. (20) into Eq. (16) yields

$$\prod = 2\sum_{i=1}^{n}\lambda_i\gamma(x_i,x) - \sum_{i=1}^{n}\sum_{j=1}^{n}\lambda_i\lambda_j\gamma(x_i,x_j) + 2\sum_{l=1}^{m}\mu_l[\sum_{i=1}^{n}\lambda_i p_l(x_i) - p_l(x)] \tag{21}$$

All derivatives of Eq. (21) with respect to $\lambda_i(x)$ and $\mu_i(x)$ must be equal to zero according to the minimum variance

$$\begin{aligned}\frac{\partial\Pi}{\partial\lambda_i} &= 2\gamma(x,x_i) - 2\sum_{j=1}^{n}\lambda_j\gamma(x_i,x_j) + 2\sum_{l=1}^{m}\mu_l p_l(x_i) = 0 \quad 1\le i\le n\\ \frac{\partial\Pi}{\partial\mu_l} &= \sum_{i=1}^{n}\lambda_i p_l(x_i) - p_l(x) = 0 \quad 1\le l\le m\end{aligned} \tag{22}$$

For simplification, Eq. (22) is rewritten into a matrix form,

$$\mathbf{GW} = \mathbf{g} \tag{23}$$

in which

$$\mathbf{G} = \begin{bmatrix}\mathbf{R} & \mathbf{P}\\ \mathbf{P}^T & \mathbf{0}\end{bmatrix} \tag{24}$$

$$\mathbf{R} = \begin{bmatrix}\gamma(x_1,x_1) & \cdots & \gamma(x_1,x_n)\\ \cdots & \cdots & \cdots\\ \gamma(x_n,x_1) & \cdots & \gamma(x_n,x_n)\end{bmatrix} \tag{25}$$

$$\mathbf{P} = \begin{bmatrix}p_1(x_1) & \cdots & p_m(x_1)\\ \cdots & \cdots & \cdots\\ p_1(x_n) & \cdots & p_m(x_n)\end{bmatrix} \tag{26}$$

$$\mathbf{W} = \begin{bmatrix}\lambda_1 & \lambda_2 & \cdots & \lambda_n & \mu_1 & \mu_2 & \cdots & \mu_m\end{bmatrix} \tag{27}$$

$$\mathbf{g}^T = \begin{bmatrix}\mathbf{r}^T(x) & \mathbf{p}^T(x)\end{bmatrix} \tag{28}$$

$$\mathbf{r}^T(x) = [\gamma(x,x_1) \quad \cdots \quad \gamma(x,x_n)] \tag{29}$$

$$\mathbf{p}^T(x) = [p_1(x) \quad \cdots \quad p_m(x)] \tag{30}$$

Using Eqs. (10) and (23), the approximate field function can be numerically calculated by

$$\hat{u}(x) = \mathbf{p}^T(x)\hat{\boldsymbol{\beta}} + \mathbf{r}^T(x)\mathbf{R}^{-1}(\mathbf{u} - \mathbf{P}\hat{\boldsymbol{\beta}}) \tag{31}$$

in which

$$\hat{\boldsymbol{\beta}} = (\mathbf{P}^T \mathbf{R}^{-1} \mathbf{P})^{-1} \mathbf{P}^T \mathbf{R}^{-1} \mathbf{u} \tag{32}$$

The interpolated function $\hat{u}(x)$ can be expressed in terms of the field value $u(x)$ by the MK interpolation

$$\begin{aligned} \hat{u}(x) &= \mathbf{p}^T(x_i)\hat{\boldsymbol{\beta}} + \mathbf{r}^T(x_i)\mathbf{R}^{-1}(\mathbf{u}(x_i) - \mathbf{P}\hat{\boldsymbol{\beta}}) \\ &= [\mathbf{p}^T(x_i)\mathbf{A} + \mathbf{r}^T(x_i)\mathbf{B}]\mathbf{u}(x_i) \\ &= \boldsymbol{\Phi}(x)\mathbf{u}(x) \end{aligned} \tag{33}$$

with $\boldsymbol{\Phi}(x)$ being the constructed MK interpolation.

$$\boldsymbol{\Phi}(x) = \mathbf{p}^T(x)\mathbf{A} + \mathbf{r}^T(x)\mathbf{B} \tag{34}$$

$$\mathbf{u}(x) = [u(x_1) \quad u(x_2) \quad \cdots \quad u(x_n)] \tag{35}$$

$$\mathbf{A} = (\mathbf{P}^T \mathbf{R} \mathbf{P})^{-1} \mathbf{P}^T \mathbf{R}^{-1} \tag{36}$$

$$\mathbf{B} = \boldsymbol{R}^{-1}(\mathbf{I} - \boldsymbol{P}\mathbf{A}) \tag{37}$$

in which $\mathbf{I}$ is an $n \times n$ unit matrix. The first-order and second-order derivatives of the MK interpolation in Eq. (34) are expressed as

$$\boldsymbol{\Phi}_{,i}(x) = \boldsymbol{p}^T{}_{,i}(x)\mathbf{A} + \boldsymbol{r}^T{}_{,i}(x)\mathbf{B} \tag{38}$$

$$\boldsymbol{\Phi}_{,ij}(x) = \boldsymbol{p}^T{}_{,ij}(x)\mathbf{A} + \boldsymbol{r}^T{}_{,ij}(x)\mathbf{B} \tag{39}$$

It is noted that the constructed MK interpolation $\boldsymbol{\Phi}(x)$ in Eq. (34) inherently possesses the Kronecker delta property

$$\phi_i(x_j) = \delta_{ij} \tag{40}$$

Most mesh-free shape functions (e.g., moving least-squares) do not involve the Kronecker delta property. Hence, additional treatments such as penalty functions are required to be added when imposing essential boundary conditions, but the MK interpolation does not encounter this difficulty. Moreover, no inverse matrix is required through the first-order and second-order derivatives of the MK interpolation.

This enables the stability of the MK interpolation with a time-saving advantage as compared with conventional moving least-squares techniques.

2.3. Governing equation by mesh-free method

The abovementioned initial equilibrium graphene is used as a reference configuration when studying the deformation of circular graphene sheets under external field stimuli, e.g., torsional effect. The deformation process can be expressed by

$$\begin{cases} \tilde{x}_1 = x_1 + u_1 \\ \tilde{x}_2 = x_2 + u_2 \\ \tilde{x}_3 = u_3 \end{cases} \tag{41}$$

where u_1 , u_2 and u_3 are the relative displacements to its undeformed counterparts along x_1, x_2 and x_3 directions, respectively. The displacements can be accomplished by using the developed moving Kriging (MK) interpolation [27, 29, 30]

$$\hat{\mathbf{u}} = \hat{\mathbf{u}}(\hat{u}_1, \hat{u}_2, \hat{u}_3)^{\mathrm{T}} = \sum_{\mathrm{i}=1}^{n} \boldsymbol{\phi}_{\mathrm{i}} \mathbf{u}_{\mathrm{i}} = \boldsymbol{\Phi}\mathbf{U} \tag{42}$$

where $\mathbf{u}_{\mathrm{i}} = (u_{\mathrm{i}1}, u_{\mathrm{i}2}, u_{\mathrm{i}3})^{\mathrm{T}}$ is the nodal displacement, $\boldsymbol{\phi}_{\mathrm{i}}$ is the MK interpolation at the i^{th} node, and n is the total number of nodes covered in the compact support domain.

The first-order and second-order gradients are calculated by two parts

$$\tilde{\mathbf{F}} = \mathbf{F} + \hat{\mathbf{F}}, \quad \tilde{\mathbf{G}} = \mathbf{G} + \hat{\mathbf{G}} \tag{43}$$

where the first parts **F** and **G** are directly obtained by Eq. (1), and the second parts $\hat{\mathbf{F}}$ and $\hat{\mathbf{G}}$ are approximated by the MK interpolation as

$$\hat{\mathbf{F}} = \sum_{i=1}^{n} \phi_{i,\mathbf{X}} u_i \tag{44}$$

$$\hat{\mathbf{G}} = \sum_{i=1}^{n} \phi_{i,\mathbf{XX}} u_i \tag{45}$$

in which $\phi_{i,\mathbf{X}}$ and $\phi_{i,\mathbf{XX}}$ are the first-order and second-order derivatives of the MK interpolation with respect to the reference configuration, respectively.

The total energy of the system calculated by the higher-order gradient theory can be written as

$$E = \int_{\Omega} W(\tilde{\mathbf{F}}, \tilde{\mathbf{G}}) \mathrm{d}V - \int_{\partial\Omega} \mathbf{u} \cdot \mathbf{t}_0^{\mathrm{P}} \mathrm{d}S - \int_{\partial\Omega} \nabla_{\mathrm{N}} \mathbf{u} \cdot \mathbf{t}_0^{\mathrm{Q}} \mathrm{d}S \tag{46}$$

where $\mathbf{t}_0^{\mathrm{P}}$ and $\mathbf{t}_0^{\mathrm{Q}}$ denote the first-order stress traction and the second-order stress traction on the domain surface, respectively. The outward normal gradient is $\nabla_{\mathrm{N}} \mathbf{u} = N_{X_1} \Phi_{,\mathrm{X}_1} \mathbf{u} + N_{X_2} \Phi_{,X_2} \mathbf{u}$, in which N_{X_1} and N_{X_2} are the normal components of the surface in the domain along X_1 and X_2 direction, respectively. Moreover, the equilibrium configuration of graphene under an external load should be determined by the variation of the total energy of the system. The weak form of the system can be expressed by

$$\int_{\Omega} \delta \mathbf{grad}^{\mathrm{T}} \cdot \boldsymbol{\sigma} \mathrm{d}V - \int_{\partial\Omega} \delta \mathbf{u}^{\mathrm{T}} \cdot \mathbf{t}_0^{\mathrm{P}} \mathrm{d}S - \int_{\partial\Omega} (\nabla_{\mathrm{N}} \delta \mathbf{u}) \cdot \mathbf{t}_0^{\mathrm{Q}} \mathrm{d}S = 0 \tag{47}$$

where $\boldsymbol{\sigma} = \dfrac{\partial \omega}{\partial \mathbf{grad}}$ with $\mathbf{grad} = [\tilde{\mathbf{F}} \quad \tilde{\mathbf{G}}]$.

Denote the combination of the first-order and second-order derivations with respect to the reference configuration as the following operator $\mathbf{L}$, we have

$$\mathbf{L} \cdot \boldsymbol{\Phi} = \begin{bmatrix} \boldsymbol{\Phi}_{,\mathbf{X}} \\ \boldsymbol{\Phi}_{,\mathbf{XX}} \end{bmatrix} \tag{48}$$

Hence, the incremental equation of the system can be derived as:

$$\int_{\Omega} [(\mathbf{L} \cdot \boldsymbol{\Phi})^{\mathrm{T}} \cdot \mathbf{M} \cdot (\mathbf{L} \cdot \boldsymbol{\Phi})] \Delta \mathbf{U} \mathrm{d}V = -\int_{\Omega} (\mathbf{L} \cdot \boldsymbol{\Phi})^{\mathrm{T}} \cdot \boldsymbol{\sigma}_{\mathrm{n}} \mathrm{d}V + \int_{\partial\Omega} \boldsymbol{\Phi}^{\mathrm{T}} \mathbf{t}_0^{\mathrm{P}} \mathrm{d}S + \int_{\partial\Omega} (N_1 \boldsymbol{\Phi}_{,1} + N_2 \boldsymbol{\Phi}_{,2})^{\mathrm{T}} \cdot \mathbf{t}_0^{\mathrm{Q}} \mathrm{d}S \tag{49}$$

in which $\mathbf{K} = \int_{\Omega} \left[(\mathbf{L} \cdot \mathbf{\Phi})^{\mathrm{T}} \cdot \mathbf{M} \cdot (\mathbf{L} \cdot \mathbf{\Phi}) \right] dV$ and $\mathbf{f} = -\int_{\Omega} (\mathbf{L} \cdot \mathbf{\Phi})^{\mathrm{T}} \cdot \boldsymbol{\sigma}_{\mathrm{n}} \mathrm{d}V + \int_{\partial\Omega} \mathbf{\Phi}^{\mathrm{T}} \mathbf{t}_0^{\mathrm{P}} \mathrm{d}S + \int_{\partial\Omega} (N_1 \mathbf{\Phi}_{,1} + N_2 \mathbf{\Phi}_{,2})^{\mathrm{T}} \cdot \mathbf{t}_0^{\mathrm{Q}} \mathrm{d}S$. After iteratively solving the incremental equation until the non-equilibrium force **f** reaches to zero, the equilibrium configuration of graphene under the external load can be finally obtained.

3. Numerical results and discussion

Surface morphology control is an intensive topic in nanoscience and nanotechnology. Periodic wrinkles have been observed from the shear deformation of rectangular graphene sheets and the amplitude and wavelength can be tuned by controlling the shear displacement [14]. In this section, special wrinkles can be produced at a circular graphene by imposing a torsional moment. To consider the single global controllability of surface morphology, the relevant work was conducted to control the shear displacement of rectangular graphene sheets [14]. The present twisting circular graphene is much more flexible, which can realize a continuous change of surface morphology in terms of wavenumber and amplitude.

From a simple perspective, one superiority of the present atomistic-continuum multiscale method over continuum mechanics is that it can effectively prevent the controversial issue for the thickness of a single-layer graphene sheet. Scattered values for the thickness of a single-layer graphene sheet yield the dispersive elastic properties and the system stiffness in continuum mechanics. In the present atomistic-continuum multiscale method, the atomic interaction is directly deduced by the stress-strain relationship to extract the elastic properties. The system stiffness in

Eq. (49) is only a function of the tangential moduli in Eq. (7). Apparently, the system stiffness matrix can be constructed without introducing the moment of inertia and the thickness.

On the other hand, both material and geometric nonlinearities can be captured by this atomistic-continuum multiscale method. As mentioned before, the atomic interaction is directly obtained from the constitutive relationship, and thus the real stress-strain relationship can be captured. The effect of geometric nonlinearity is described by the second-order gradient tensor in the higher-order gradient theory. The involved second-order gradient tensor can capture the bending effect, and thus it can map a more accurate vector rather than a tangent vector to perfectly approximate the real placement. Hence, both material and geometric nonlinearities can be reflected by iteratively updating the system stiffness matrix in Eq. (49) when studying the large deformation of graphene.

Figure 2 shows the schematic diagrams of a clamped circular graphene analyzed by two approaches, i.e., atomistic-continuum multiscale method and full atomistic simulation approach. The nodes labeled in red are completely fixed, and a torsional moment along the z direction is applied to those nodes labeled in green. A twisting angle loading of 1° per each step is imposed at the green region around the center node. Indeed, the nodal arrangement plays a significant role on the accuracy of a mesh-free computational framework. A uniformly distributed nodal arrangement scheme in the whole domain is a perfect choice. To perform this task, n and $6i$ nodes with i being 1,…, n-1, along the radial and circumferential directions respectively, are

arranged as shown in Fig. 2. Such an arrangement ensures the equivalent radial and circumferential distance between neighboring nodes, with a total number of $3n(n-1)+1$ nodes.

3.1. Verification of the convergence and efficiency of atomistic-continuum method

Firstly, a series of case studies are provided to show the accuracy of the present atomistic-continuum multiscale method on the nodal arrangement. A torsional moment is applied to the green zone $\rho \le r_{\mathrm{I}}$ and the red zone $\rho \ge R_{\mathrm{o}}$ is completely fixed. A circular graphene sheet with $R_{\mathrm{o}} = 3$ nm under various inner radii ($r_{\mathrm{I}} = 0.5$, 1.0 and 1.5 nm) is considered. Four different nodal arrangement schemes I - IV, i.e., n = 8, 14, 20 and 26, respectively, are presented. These four computational schemes, corresponding to the total number of 169, 547, 1141 and 1951 nodes, are used to verify the present atomistic-continuum multi-scale method. The total number of atoms of this circular graphene sheet can be determined from a continuum viewpoint, namely, dividing the surface area $\pi \times R_{\mathrm{o}}^2$ to the average area per atom $3\sqrt{3}r^2/4$, where r is the C-C bond length in the initial equilibrium configuration of graphene. In the present simulation, the initial C-C bond length is determined to be 0.14507 nm and thus there are a total number of at least 1034 atoms.

Both amplitude and wavenumber are two important factors to control the surface morphology of graphene. Figure 3 shows the relationship between the computational amplitude of wrinkles and the imposed torsional angles. As shown in Fig. 3(a), all the wrinkle amplitude-torsional angle curves show that a distinct wrinkle for a circular

graphene with R_o = 3 nm and r_I = 0.5 nm starts to be generated under an external torsional angle ≥3°. When only a few number of nodes in Scheme I (i.e., n = 8) are used, the amplitude of wrinkles will be under-estimated. This tendency becomes increasingly severe as the torsional angle increases. It is noteworthy that other three arrangement schemes (II – IV) nearly offer the same prediction for the amplitude of wrinkles. This means that the nodal arrangement in Scheme I is too sparse, it cannot catch the detailed information. By increasing the values of n in Schemes II-IV, the computational results will be well convergent. To increase r_I, the same conclusion can also be drawn from the analysis in Fig. 3(b) and Fig. 3(c). Both figures show that the computational results obtained by Scheme I cannot provide good agreement with other three schemes. When n is not less than 14, the present atomistic-continuum multiscale method can give a steady and good prediction for the torsional behaviour of circular graphene sheets. In this case, nearly half degrees of freedom can be reduced as compared with the atomistic simulation method.

In order to further demonstrate the ability of catching the detailed information in the whole domain, we consider the average out-of-displacement that is defined by dividing the sum of the nodal out-of-displacement by the number of nodes in the deformed region. In Figs. 4(a)-(c), the curves show the deviation of Scheme I with respect to other three schemes, although the amplitude of wrinkle-torsional angle curves in Fig. 3(b) and Fig. 3(c) seem to be much closer to each other. In reality, this fake closeness is due to different patterns, only three and four wrinkles, respectively, are caught in Scheme I (not shown) while in fact that there are four and five wrinkles

in Schemes II-IV (as shown in Fig. 9(c) and Fig. 9(e)). Such a close average out-of-displacement for Schemes II-IV confirms again that the detailed deformation can be exactly caught when $n \geq 14$.

To verify the accuracy of the present atomistic-continuum multiscale method, a full atomistic simulation on the torsional behaviour of a circular graphene sheet with R_o=3 nm and r_I=1.5 nm is also carried out (see Fig. 2). The variation of the amplitude and wrinkle patterns under various torsional angles is provided in Figs. 5(a)-(c). The curves obtained by these two methods are coincident with each other, as shown in Fig. 5(a). The onset torsional angle on the formation of wrinkles is conformably determined to be 3^o in both full atomistic simulation and atomistic-continuum multiscale method. Using the full atomistic simulation, it is impossible to construct a strict circular graphene and to impose a torsional moment on a circular region. Hence, this yields a slight deviation between these two methods. Figure 5(b) shows the wrinkle patterns obtained by both methods. The results show that five fins are generated. Nevertheless, the wrinkle pattern obtained by the full atomistic simulation is not quite symmetric to that obtained by the atomistic-continuum approach. It is because the discrete hexagonal structure is not a circular symmetry, and thus it is not easy to impose a symmetric load on the boundary constraints. In Fig. 5(c), it is found that the effect of the structural asymmetry on the torsional behaviour of circular graphene sheets becomes smaller as the twisting angle increases. The wrinkle pattern as well as the amplitude at a twisting angle of 8^o captured by the atomistic-continuum approach is in good agreement with those obtained by the full atomistic simulation.

Due to the limitations of the full atomistic simulation, the atomistic-continuum multiscale method is more flexible and applicable for the analysis of circular graphene sheets, in terms of both computational effort and numerical accuracy.

The above numerical simulations exhibit good accuracy and convergence of the atomistic-continuum multiscale method. However, all these case studies are for the research sample with a radius of 3 nm. To illustrate the validity of the same setting for large-sized graphene sheets, two-fold and three-fold samples are selected for numerical analysis, i.e., R_o = 6 nm and 9 nm, with the total number of 4136 and 9306 atoms, respectively. The relationship between the amplitude, average out-of-displacement and torsional angle is presented in Fig. 6 and Fig. 7. It is similar to the previous case, these two figures also show good convergence except Scheme I. Moreover, these two studies further confirm the universal feasibility of the present atomistic-continuum approach, especially it exhibits a remarkable superiority in saving computational resource. For example, Scheme II uses a total number of 547 nodes, with only 1/8 and 1/17 degrees of freedom of those full atomistic simulations for the cases of R_o= 6 nm and 9 nm, respectively. In the subsequent studies, Scheme II will be adopted due to its computational effort and numerical accuracy, unless otherwise specified.

3.2. Parametric study and twisting patterns of circular graphene sheets

A parametric study is conducted to investigate the effects of the torsional moment, outer radius R_o and inner radius r_I on the formation of wrinkles. The numerical results

for circular graphene sheets are given in Fig. 8. In Fig. 8(a), the wrinkle formation onset torsional angle decreases as the inner radius r_I increases, while the amplitude has a generally increasing tendency except r_I=1.5 nm. The average out-of-displacement of wrinkles plotted in Fig. 8(b) shows that the change of curves r_I = 0.5 nm, 0.75 nm and 1.25 nm are parallel, while the rest two curves have many intersections, especially for r_I=1.5 nm. This scenario is due to the sudden change of the wrinkle patterns. In addition, the increment in the amplitude becomes smaller as the torsional angle increases. Figure 9 depicts the wrinkle patterns of all these five kinds of graphene sheets. As r_I increases from 0.5 nm to 1.5 nm, the wrinkle wavenumber of graphene also increases. This yields a reduction effect on the amplitude of wrinkles. Another reason is that the length of the distorted wrinkle along the radial direction becomes smaller to make a stronger restriction on the amplitude as r_I increases. In Fig. 8(c), it is also noteworthy that the strain energy monotonously and distinctly increases as r_I increases. Although there is a sudden change in surface morphology, there is no energy jump apparently. Hence, it is a fully elastic unloaded and reloaded process. Reversible and controllable wrinkles can be realized by loading and unloading, which is consistent with the superelastic property [15].

In Fig. 9, the results are similar to those obtained in Fig. 8. However, Fig. 10(a) and Fig. 10(b) show that the five curves intertwine with each other as compared with Fig. 8(a) and Fig. 8(b). In addition, the wrinkle formation onset torsional angle decreases as the size of graphene samples increases. Moreover, there are amplitude jumps in the cases of r_I = 2.0 nm, 2.5 nm and 3.0 nm. Figure 10(c) also indicates that

the strain energy monotonously and distinctly increases as r_I increases. Figure 11 plots the variation of wrinkle patterns for clamped circular graphene sheets with R_o = 6 nm, in which the wavenumbers are generally the same as those presented in Fig. 9.

Based on the results presented in Fig. 8, Fig. 10 and Fig. 12, it is concluded that the wrinkle formation onset torsional angle becomes smaller as the graphene radius increases. The same intertwining phenomenon occurs in Fig. 12(a) and Fig. 12(b). It is also found that the wavenumber generally increases as the graphene sample size increases. Figure 13 depicts the variation of wrinkle patterns for clamped circular graphene sheets with R_o = 9 nm .

In Fig. 14(a) and Fig. 14(b), it is found that both r_I and R_o have a positive effect on the wavenumber, while they have a negative effect on the wrinkle formation onset torsional angle. To compare with the curves in Fig. 14(c), it is also found that each amplitude jump point is inevitably accompanied when increasing the wavenumber. This is a reasonable explanation to the phenomenon observed in Fig. 8.

As aforementioned, there is an abrupt jump in the amplitude-torsional angle curves in Fig. 10 and Fig. 12. This is caused by the sudden change in the wrinkle patterns as shown in Fig. 15 and Fig. 16. The patterns are not only controlled by the combination of r_I and R_o, but also it can be tuned by the torsional angle. It implies that the change of torsional angles can induce a significant effect on the amplitude and wrinkle pattern of graphene sheets.

4. Conclusions

The twisting behaviour of circular graphene sheets is investigated by the atomistic-continuum multiscale method, which can accurately capture the effects of both geometric and material nonlinearities. To compare with the full atomistic simulation approach, the present method exhibits a universal feasibility with remarkable superiority in saving computational efforts. The numerical results indicate that the amplitude of wrinkles depends on the torsional angle and the size of graphene (i.e., outer radius R_o and inner radius r_I). For a given r_I/R_o ratio, the amplitude increases as the graphene size increases. The wrinkle formation onset torsional angle decreases when the graphene size increases. For a given R_o, the wavenumber increases as r_I increases, resulting in a reduction effect on the amplitude. As the ratio r_I/R_o decreases, the length of the distorted wrinkle along the radial direction will also decrease to strongly restrict the amplitude. It is also noted that a jump will occur at the amplitude as the torsional angle continuously increases. Although there is a sudden change in the wrinkle wavenumber, energy still keeps growing. This phenomenon implies that a superelastic property can realize reversible and controllable wrinkles by loading and unloading.

Acknowledgements

The work described in this paper was fully supported by the research grants from Natural Science Foundation of China (Grant Nos. 11702112 and 11602210), Natural Science Foundation of Guangdong Province (Nos. 2016A030310090 and 2017A030310183) and Open Project of Key Laboratory for Strength and Vibration of Mechanical Structures (SV2017-KF-23). The funding support of the Early Career Scheme (Project No. PolyU 252026/16E) from the Research Grants Council of the Hong Kong Special Administrative Region is also acknowledged.

References

[1] K.S. Novoselov, A.K. Geim, S.V. Morozov, D. Jiang, Y. Zhang, S.V. Dubonos, I.V. Grigorieva, A.A. Firsov, Electric field effect in atomically thin carbon films, Science, 306 (2004) 666-669.

[2] K.S. Novoselov, D. Jiang, F. Schedin, T.J. Booth, V.V. Khotkevich, S.V. Morozov, A.K. Geim, Two-dimensional atomic crystals, P Natl Acad Sci USA, 102 (2005) 10451-10453.

[3] C. Lee, X.D. Wei, J.W. Kysar, J. Hone, Measurement of the elastic properties and intrinsic strength of monolayer graphene, Science, 321 (2008) 385-388.

[4] F. Schwierz, Graphene transistors, Nat Nanotechnol, 5 (2010) 487-496.

[5] J.C. Meyer, A.K. Geim, M.I. Katsnelson, K.S. Novoselov, T.J. Booth, S. Roth, The structure of suspended graphene sheets, Nature, 446 (2007) 60-63.

[6] A. Fasolino, J.H. Los, M.I. Katsnelson, Intrinsic ripples in graphene, Nat Mater, 6 (2007) 858-861.

[7] Y.J. Wei, B.L. Wang, J.T. Wu, R.G. Yang, M.L. Dunn, Bending Rigidity and Gaussian Bending Stiffness of Single-Layered Graphene, Nano Lett, 13 (2013) 26-30.

[8] Y.Y. Liu, B.I. Yakobson, Cones, Pringles, and Grain Boundary Landscapes in Graphene Topology, Nano Lett, 10 (2010) 2178-2183.

[9] W.Z. Bao, F. Miao, Z. Chen, H. Zhang, W.Y. Jang, C. Dames, C.N. Lau, Controlled ripple texturing of suspended graphene and ultrathin graphite membranes, Nat Nanotechnol, 4 (2009) 562-566.

[10] A.L.V. de Parga, F. Calleja, B. Borca, M.C.G. Passeggi, J.J. Hinarejos, F. Guinea, R. Miranda, Periodically rippled graphene: Growth and spatially resolved electronic structure, Phys Rev Lett, 100 (2008).

[11] F. Varchon, P. Mallet, J.Y. Veuillen, L. Magaud, Ripples in epitaxial graphene on the Si-terminated SiC(0001) surface, Phys Rev B, 77 (2008).

[12] Z.J. Li, Z.G. Cheng, R. Wang, Q. Li, Y. Fang, Spontaneous Formation of Nanostructures in Graphene, Nano Lett, 9 (2009) 3599-3602.

[13] A. Capasso, E. Placidi, H.F. Zhan, E. Perfetto, J.M. Bell, Y.T. Gu, N. Motta, Graphene ripples generated by grain boundaries in highly ordered pyrolytic graphite,

Carbon, 68 (2014) 330-336.

[14] W.H. Duan, K. Gong, Q. Wang, Controlling the formation of wrinkles in a single layer graphene sheet subjected to in-plane shear, Carbon, 49 (2011) 3107-3112.

[15] C. Li, D. Jiang, H. Liang, B. Huo, C. Liu, W. Yang, J. Liu, Superelastic and Arbitrary-Shaped Graphene Aerogels with Sacrificial Skeleton of Melamine Foam for Varied Applications, Advanced Functional Materials, (2017) 1704674.

[16] H.-S. Shen, Y. Xiang, Postbuckling behavior of functionally graded graphene-reinforced composite laminated cylindrical shells under axial compression in thermal environments, Comput Method Appl M, 330 (2018) 64-82.

[17] M. Arroyo, T. Belytschko, Finite element methods for the non-linear mechanics of crystalline sheets and nanotubes, Int J Numer Meth Eng, 59 (2004) 419-456.

[18] X. Guo, J.B. Wang, H.W. Zhang, Mechanical properties of single-walled carbon nanotubes based on higher order Cauchy-Born rule, Int J Solids Struct, 43 (2006) 1276-1290.

[19] J.B. Wang, X. Guo, H.W. Zhang, L. Wang, J.B. Liao, Energy and mechanical properties of single-walled carbon nanotubes predicted using the higher order Cauchy-Born rule, Phys Rev B, 73 (2006) 115428.

[20] Y.Z. Sun, K.M. Liew, Mesh-free simulation of single-walled carbon nanotubes using higher order Cauchy-Born rule, Comp Mater Sci, 42 (2008) 444-452.

[21] Y.Z. Sun, K.M. Liew, The buckling of single-walled carbon nanotubes upon bending: The higher order gradient continuum and mesh-free method, Comput Method Appl M, 197 (2008) 3001-3013.

[22] J. Tersoff, New Empirical-Approach for the Structure and Energy of Covalent Systems, Phys Rev B, 37 (1988) 6991-7000.

[23] D.W. Brenner, Empirical Potential for Hydrocarbons for Use in Simulating the Chemical Vapor-Deposition of Diamond Films, Phys Rev B, 42 (1990) 9458-9471.

[24] K.M. Liew, Y.Z. Sun, Elastic properties and pressure-induced structural transitions of single-walled carbon nanotubes, Phys Rev B, 77 (2008) 205437.

[25] J.W. Yan, K.M. Liew, L.H. He, Free vibration analysis of single-walled carbon nanotubes using a higher-order gradient theory, Journal of Sound and Vibration, 332

(2013) 3740-3755.

[26] J.W. Yan, L.W. Zhang, K.M. Liew, A multiscale computational framework for the analysis of graphene involving geometrical and material nonlinearities, Comput Method Appl M, 310 (2016) 208-232.

[27] L. Gu, Moving kriging interpolation and element-free Galerkin method, Int J Numer Meth Eng, 56 (2003) 1-11.

[28] T.Q. Bui, M.N. Nguyen, C.Z. Zhang, A moving Kriging interpolation-based element-free Galerkin method for structural dynamic analysis, Comput Method Appl M, 200 (2011) 1354-1366.

[29] J.W. Yan, K.M. Liew, L.H. He, Analysis of single-walled carbon nanotubes using the moving Kriging interpolation, Comput Method Appl M, 229 (2012) 56-67.

[30] J.W. Yan, K.M. Liew, L.H. He, A mesh-free computational framework for predicting buckling behaviors of single-walled carbon nanocones under axial compression based on the moving Kriging interpolation, Comput Method Appl M, 247 (2012) 103-112.

Captions of Figures

Fig. 1 Initial equilibrium configuration mapping from a reference graphene by three geometrical parameters λ_1, λ_2 and θ. The branch-like structure included in the dashed square is a representative cell.

Fig. 2 Schematic diagrams of a clamped circular graphene analyzed by (a) atomistic-continuum multi-scale method and (b) full atomistic simulation. Nodes labeled in red are completely fixed, while those labeled in green are subject to a torsional moment along *z* direction.

Fig. 3 Comparison of wrinkle amplitudes for clamped circular graphene sheets (R_o=3 nm and (a) r_I = 0.5 nm , (b) r_I = 1.0 nm and (c) r_I =1.5 nm).

Fig. 4 Comparison of average out-of-displacement of wrinkles for clamped circular graphene sheets (R_o=3 nm and (a) r_I = 0.5 nm, (b) 1.0 nm and (c) 1.5 nm).

Fig. 5 Comparison of amplitudes and wrinkle patterns for clamped circular graphene sheets by full atomistic simulation and atomistic-continuum approach (R_o=3 nm and r_I = 1.5 nm).

Fig. 6 Comparison of amplitudes and average out-of-displacement (wrinkles) for clamped circular graphene sheets (R_o=6 nm and r_I=1.0 nm).

Fig. 7 Comparison of amplitudes and average out-of-displacement (wrinkles) for clamped circular graphene sheets (R_o=9 nm and r_I=1.5 nm).

Fig. 8 Effects of (a) amplitude, (b) average out-of-displacement and (c) average potential per atom of wrinkles generated by twisting clamped circular graphene sheets with outer radius of 3 nm and inner radius 0.5~1.5 nm.

Fig. 9 Variation of wrinkle patterns for clamped circular graphene sheets (R_o = 3 nm).

Fig. 10 Effects of (a) amplitude, (b) average out-of-displacement and (c) average potential of wrinkles generated by twisting clamped circular graphene sheets with outer radius of 6 nm and inner radius of 1.0~3.0 nm.

Fig. 11 Variation of wrinkle patterns for clamped circular graphene sheets (R_o = 6 nm).

Fig. 12 Effects of amplitude, average out-of-displacement and average potential of wrinkles generated by twisting clamped circular graphene sheets with outer radius of 9 nm and inner radius of 1.5~4.5 nm.

Fig. 13 Variation of wrinkle patterns for clamped circular graphene sheets (R_o = 9 nm).

Fig. 14 Effects of wavenumber, wrinkle formation onset torsional angle and amplitude for circular graphene sheets with R_o=3, 6 and 9 nm.

Fig. 15 Variation of wrinkle patterns for radial graphene sheets (R_o = 6 nm).

Fig. 16 Variation of wrinkle patterns for radial graphene sheets (R_o = 9 nm).

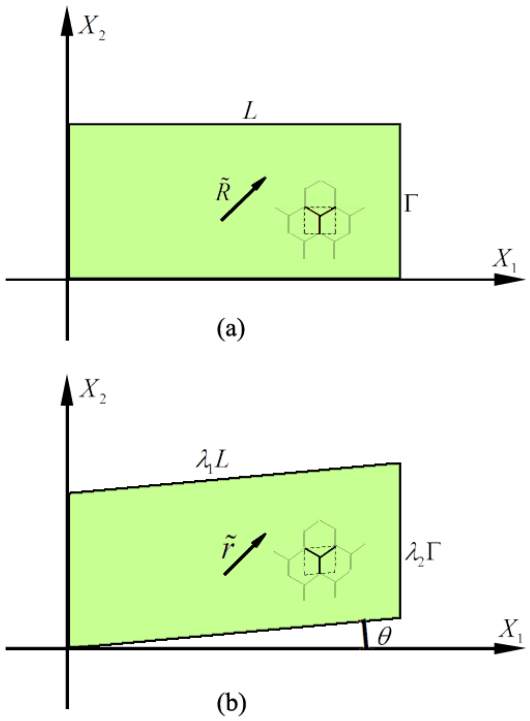

Fig. 1 Initial equilibrium configuration mapping from a reference graphene by three geometrical parameters λ_1, λ_2 and θ. The branch-like structure included in the dashed square is a representative cell.

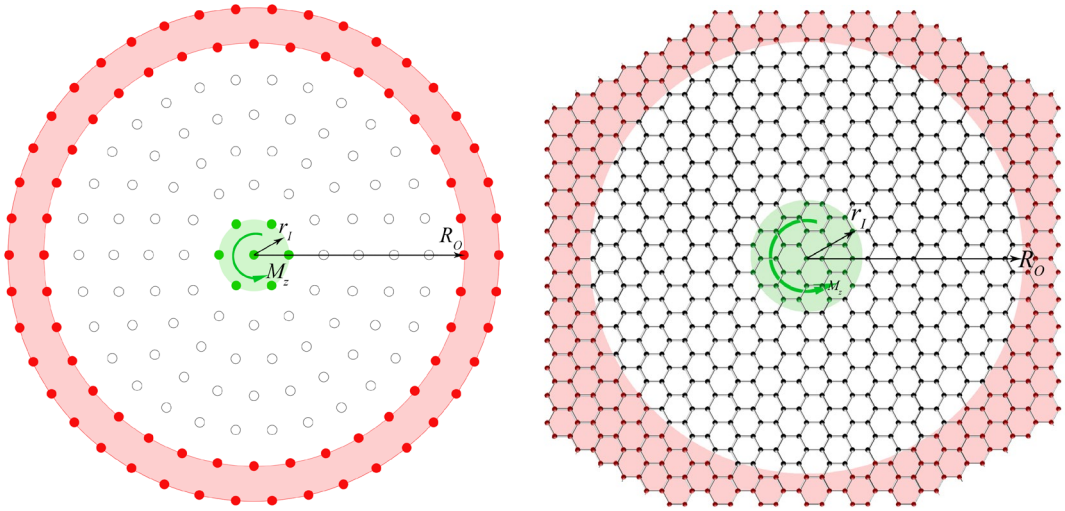

(a) (b)

Fig. 2 Schematic diagrams of a clamped circular graphene analyzed by (a) atomistic-continuum multi-scale method and (b) full atomistic simulation. Nodes labeled in red are completely fixed, while those labeled in green are subject to a torsional moment along *z* direction.

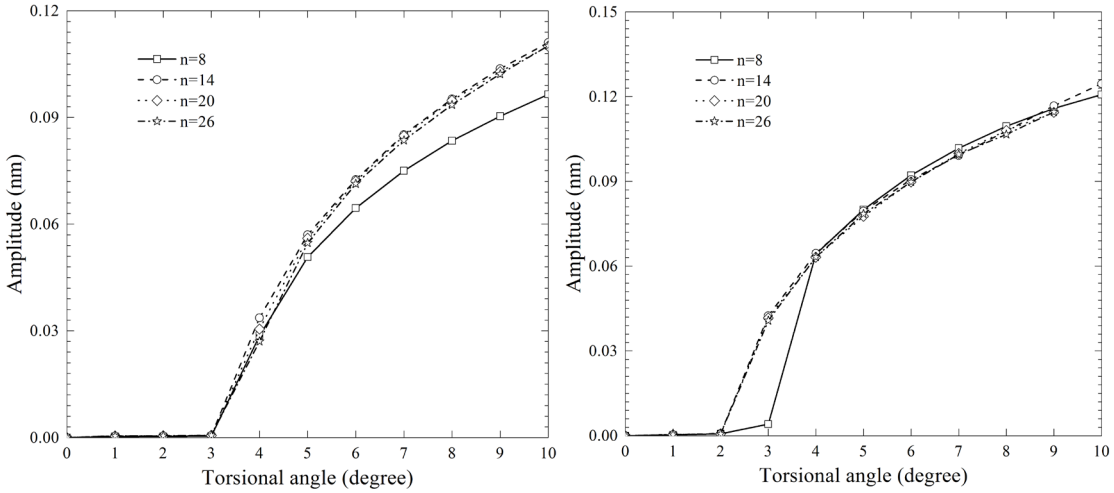

(a) (b)

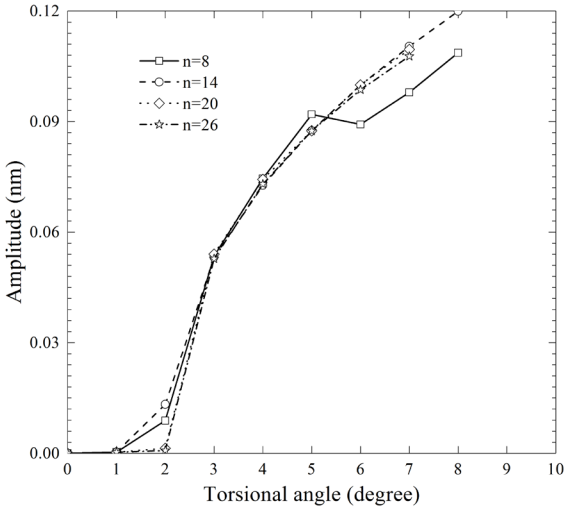

(c)

Fig. 3 Comparison of wrinkle amplitudes for clamped circular graphene sheets (R_o=3 nm and (a) r_I = 0.5 nm , (b) r_I = 1.0 nm and (c) r_I =1.5 nm).

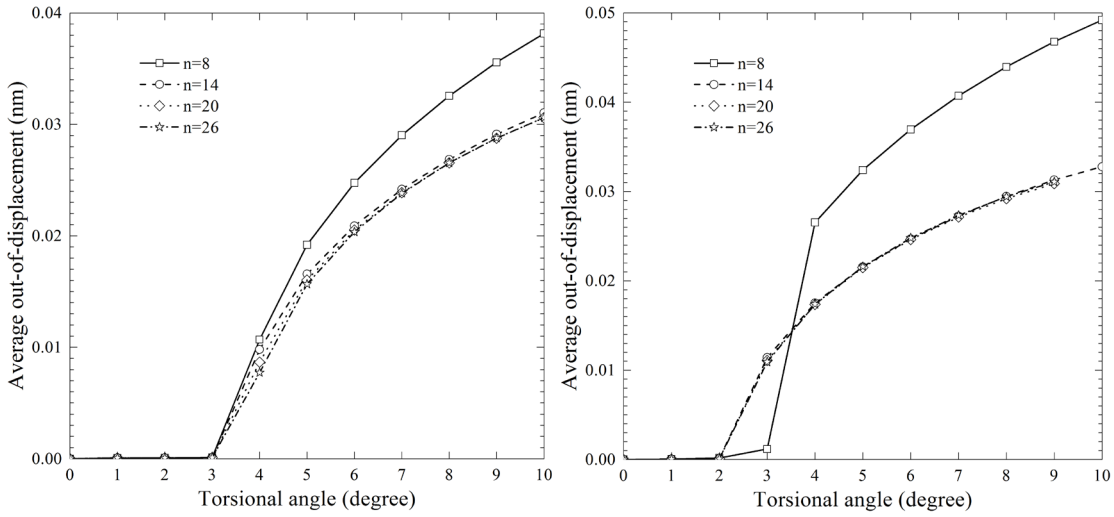

(a) (b)

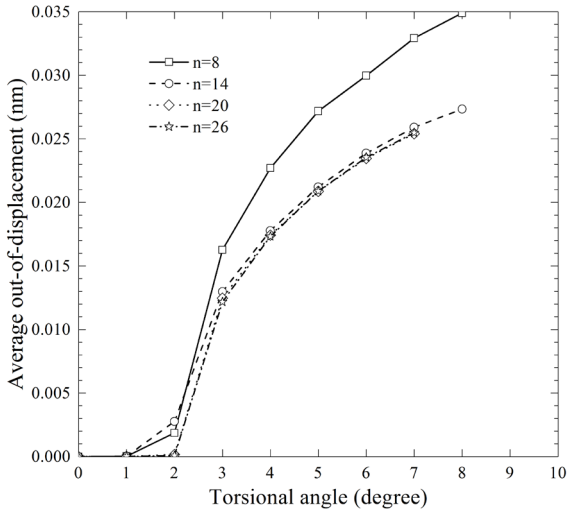

(c)

Fig. 4 Comparison of average out-of-displacement of wrinkles for clamped circular graphene sheets (R_o=3 nm and (a) r_I = 0.5 nm, (b) 1.0 nm and (c) 1.5 nm).

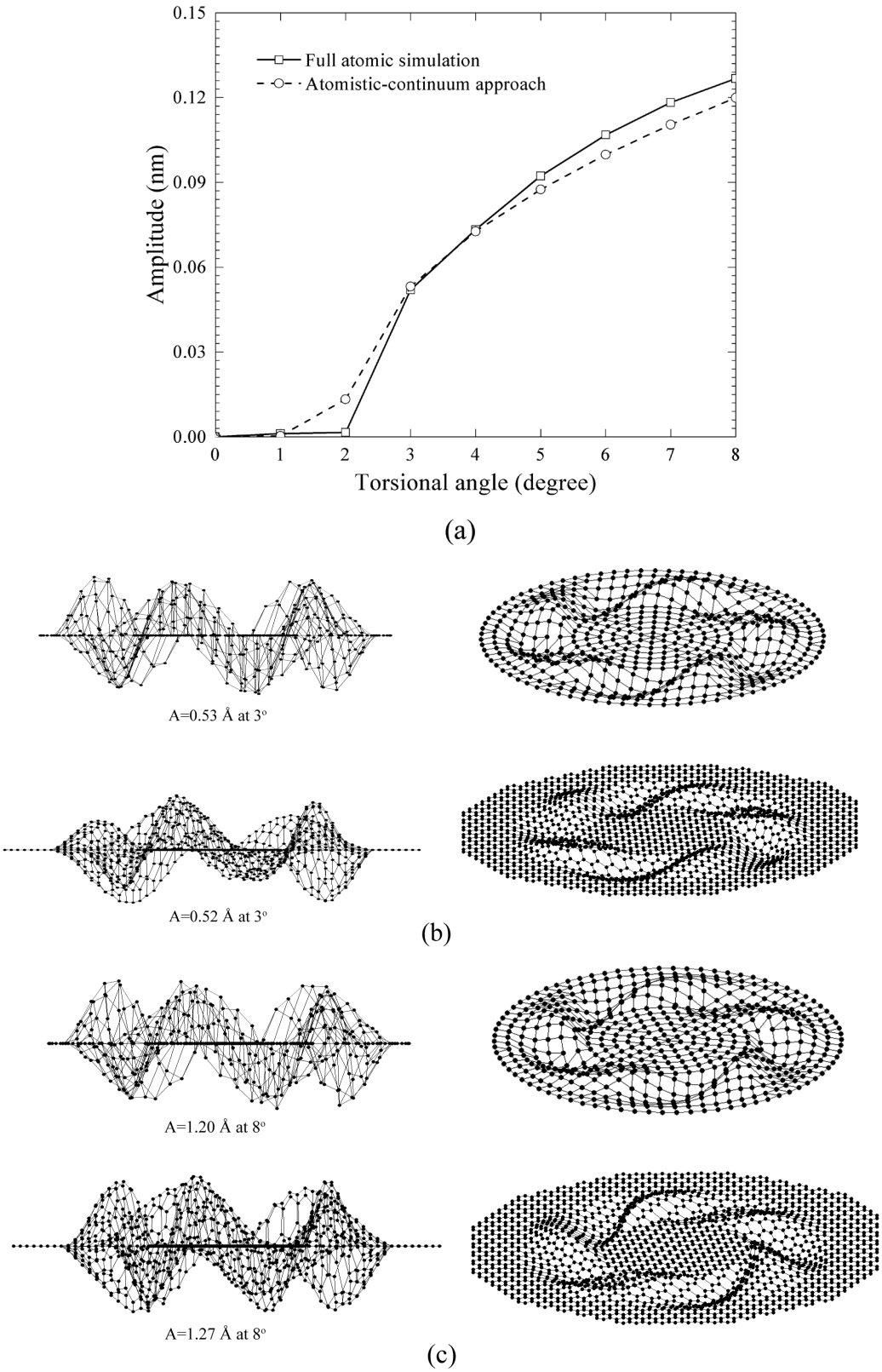

Fig. 5 Comparison of amplitudes and wrinkle patterns for clamped circular graphene sheets by full atomistic simulation and atomistic-continuum approach (R_o=3 nm and r_I = 1.5 nm).

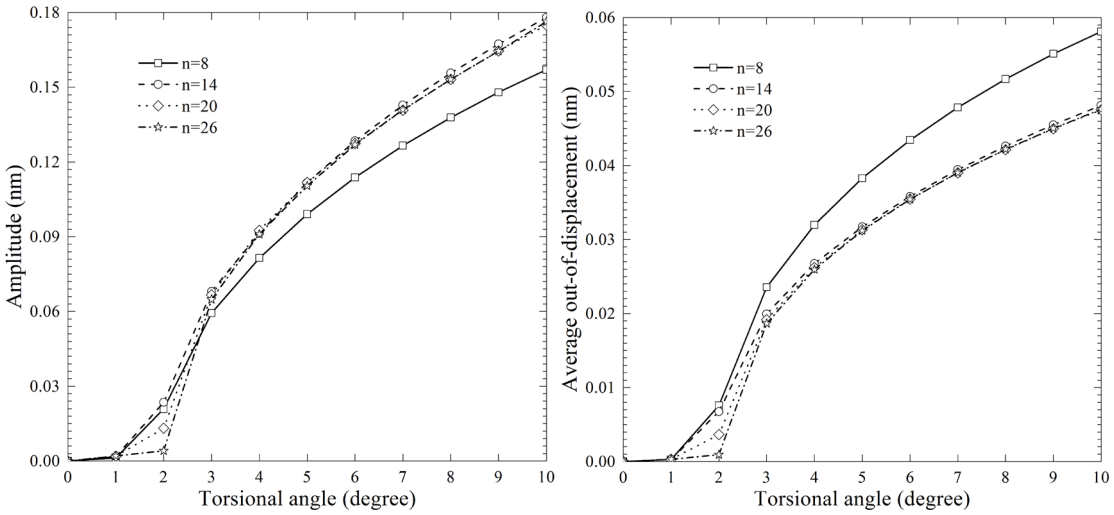

(a) (b)

Fig. 6 Comparison of amplitudes and average out-of-displacement (wrinkles) for clamped circular graphene sheets (R_o=6 nm and r_I=1.0 nm).

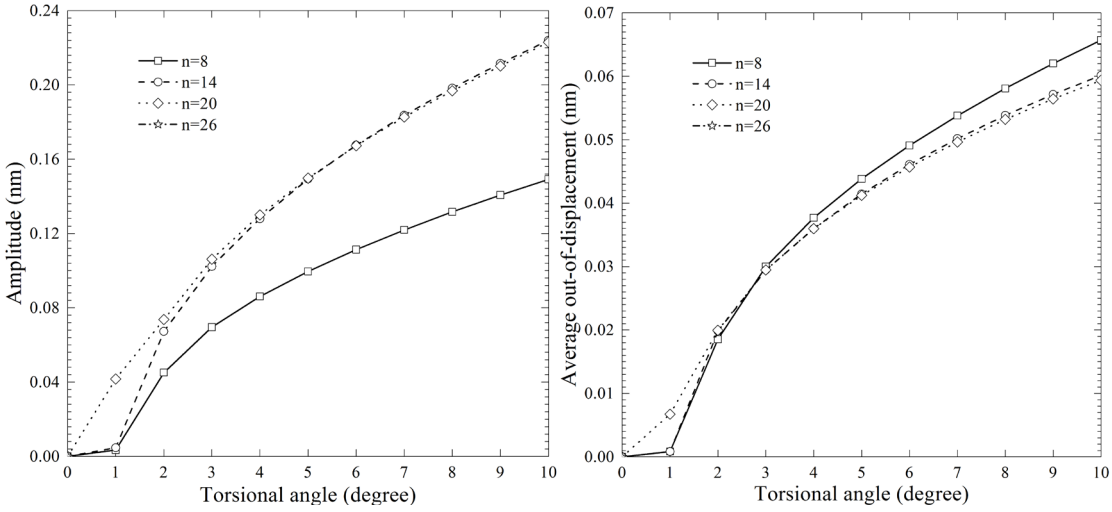

(a) (b)

Fig. 7 Comparison of amplitudes and average out-of-displacement (wrinkles) for clamped circular graphene sheets (R_o=9 nm and r_I=1.5 nm).

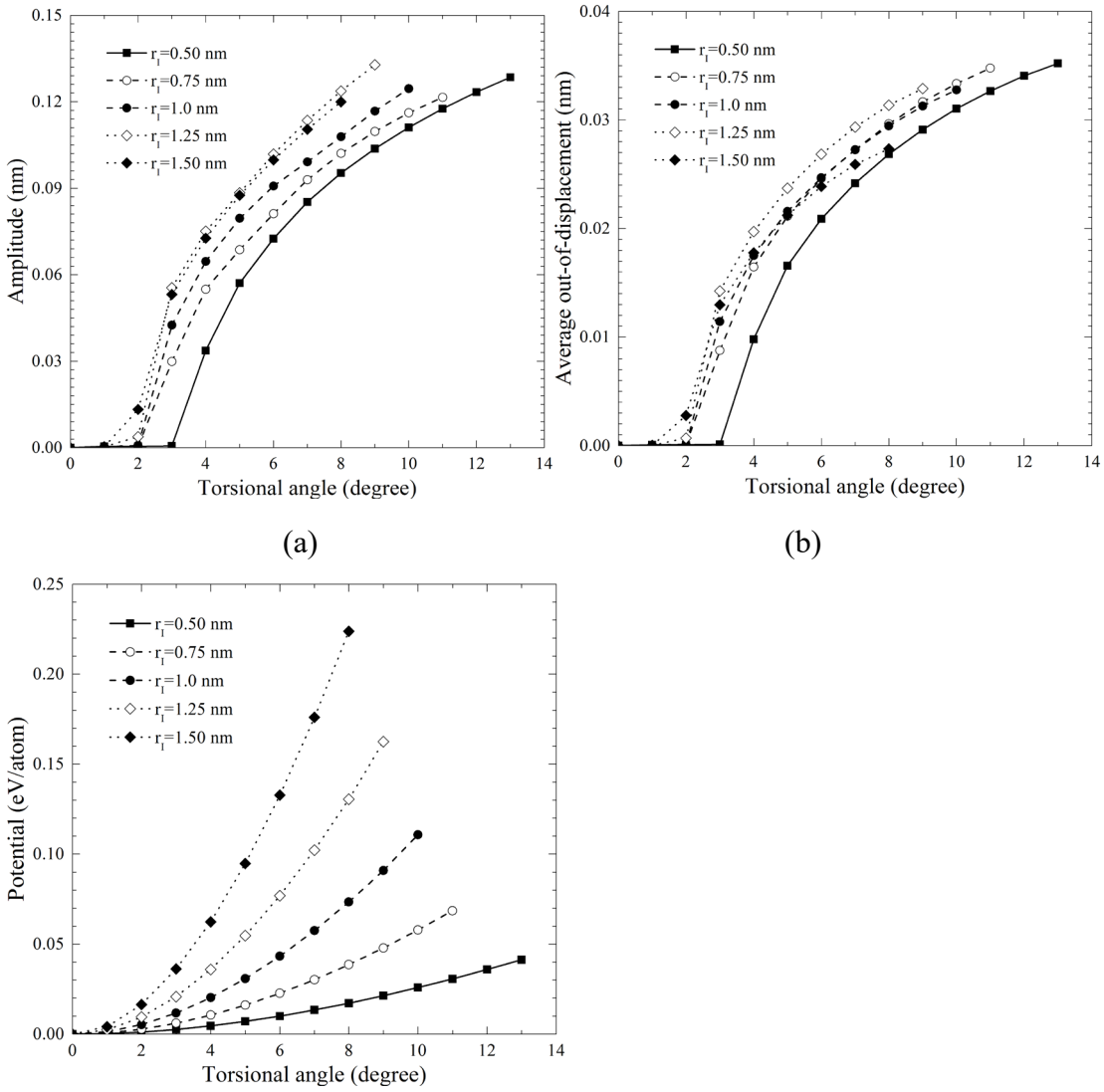

Fig. 8 Effects of (a) amplitude, (b) average out-of-displacement and (c) average potential per atom of wrinkles generated by twisting clamped circular graphene sheets with outer radius of 3 nm and inner radius 0.5~1.5 nm.

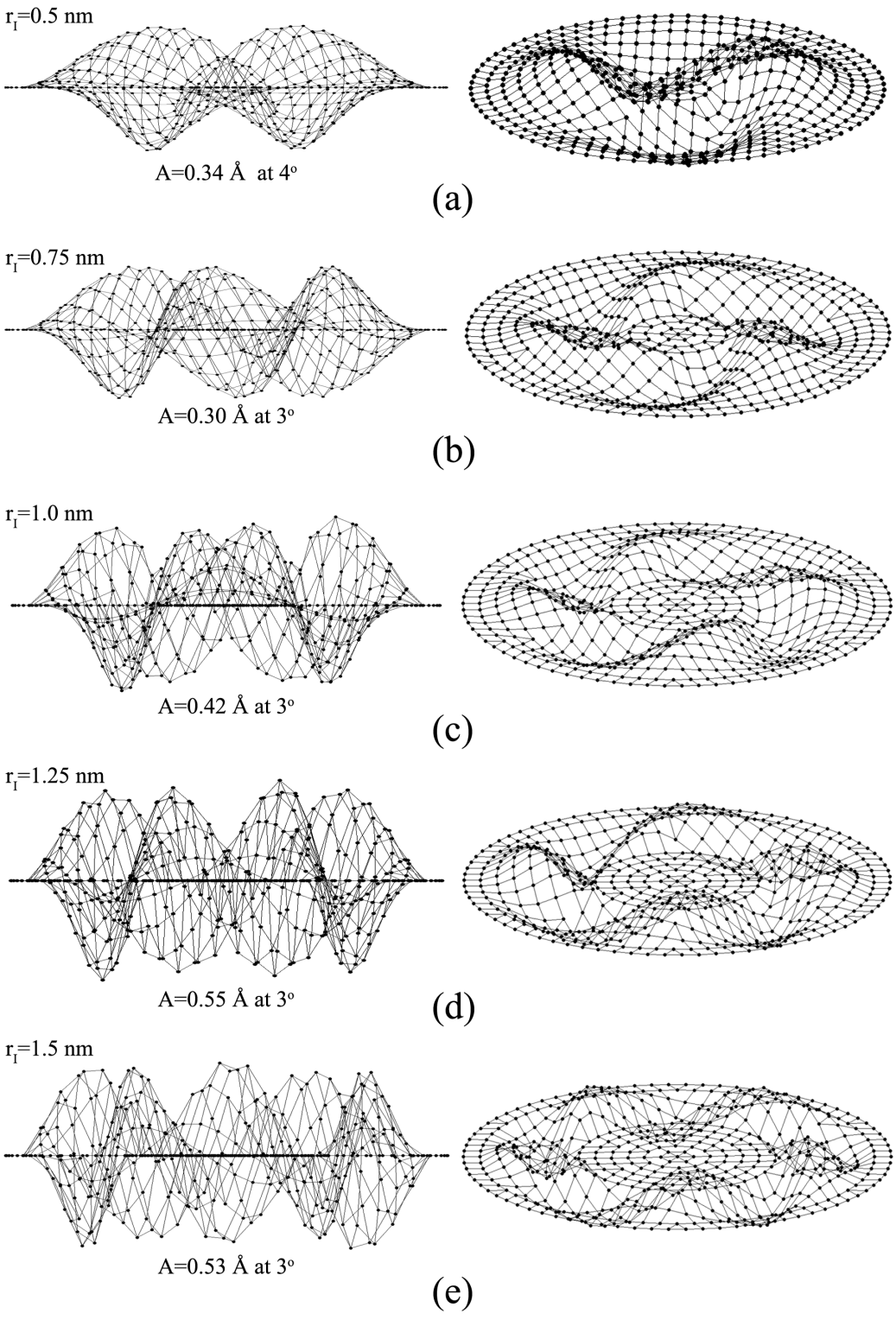

Fig. 9 Variation of wrinkle patterns for clamped circular graphene sheets (R_o = 3 nm).

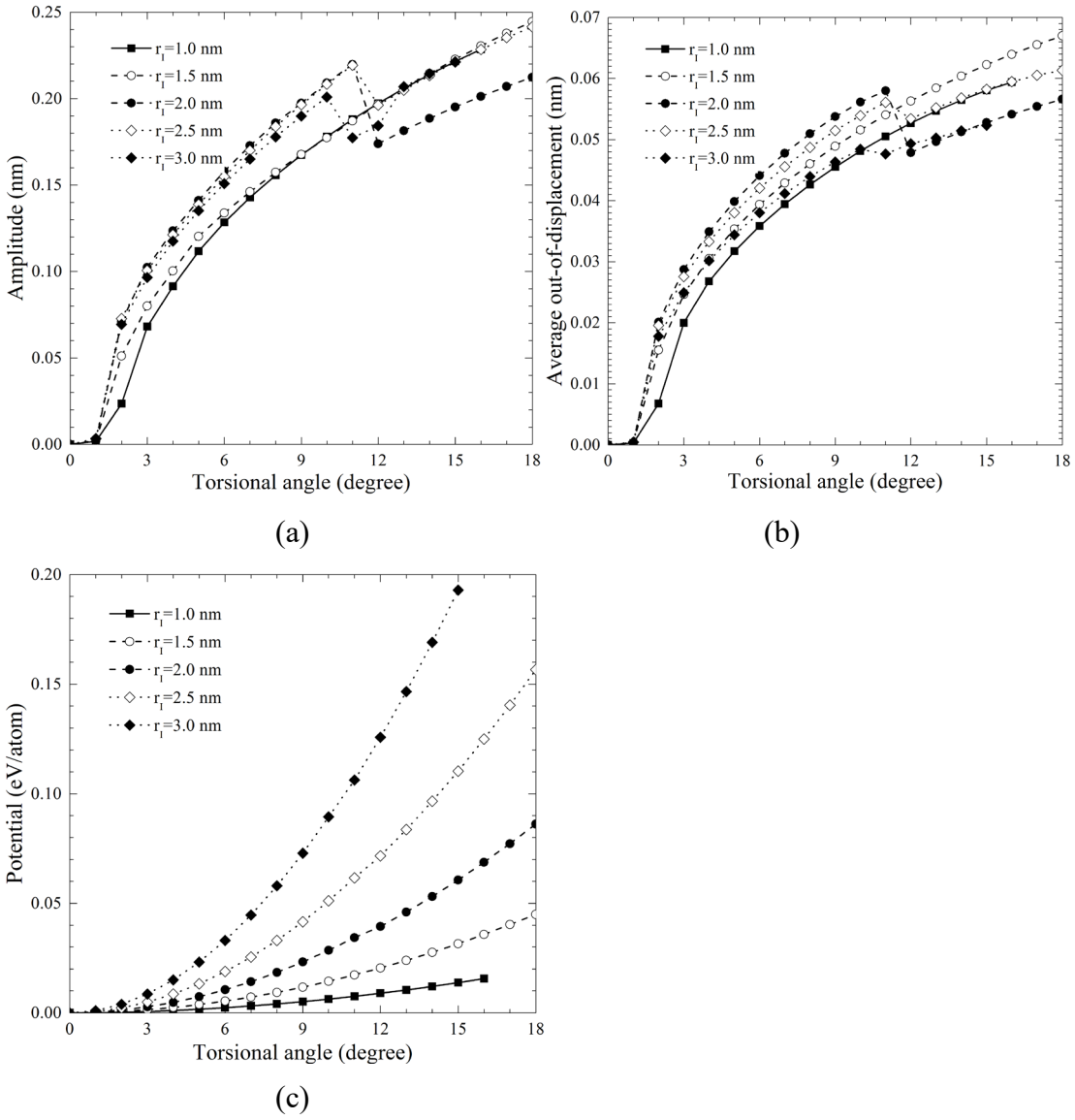

Fig. 10 Effects of (a) amplitude, (b) average out-of-displacement and (c) average potential of wrinkles generated by twisting clamped circular graphene sheets with outer radius of 6 nm and inner radius of 1.0~3.0 nm.

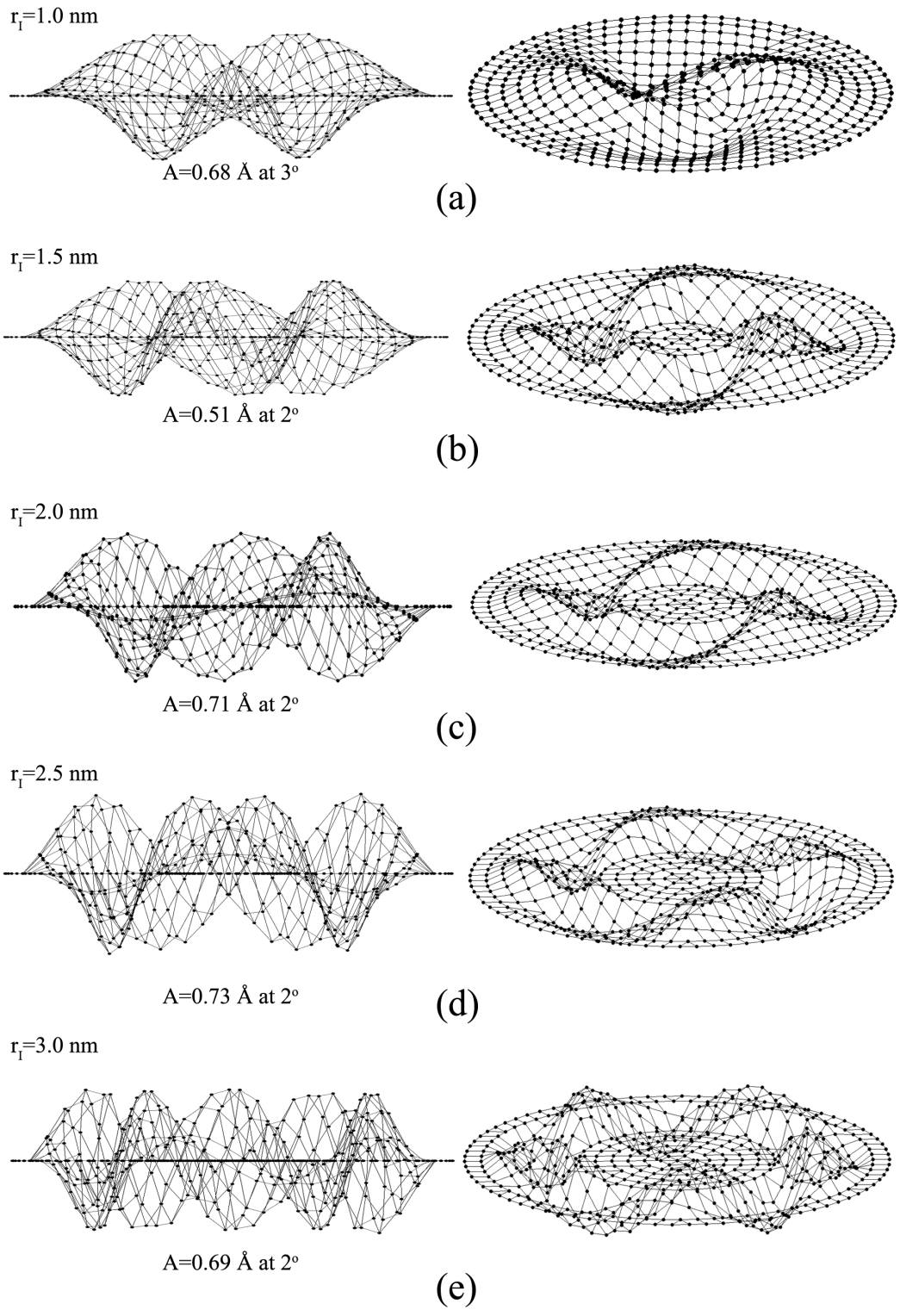

Fig. 11 Variation of wrinkle patterns for clamped circular graphene sheets (R_o = 6 nm).

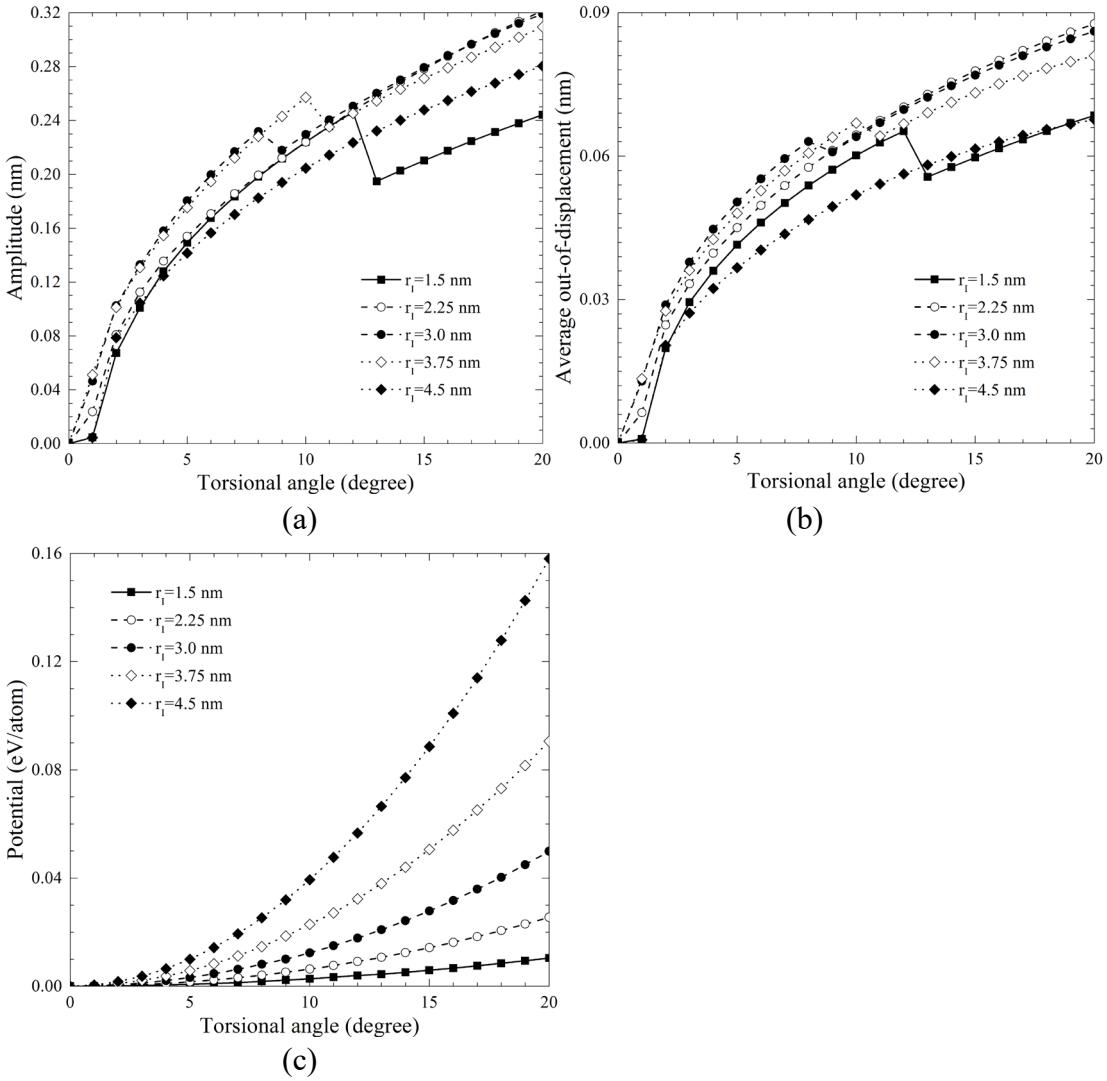

Fig. 12 Effects of amplitude, average out-of-displacement and average potential of wrinkles generated by twisting clamped circular graphene sheets with outer radius of 9 nm and inner radius of 1.5~4.5 nm.

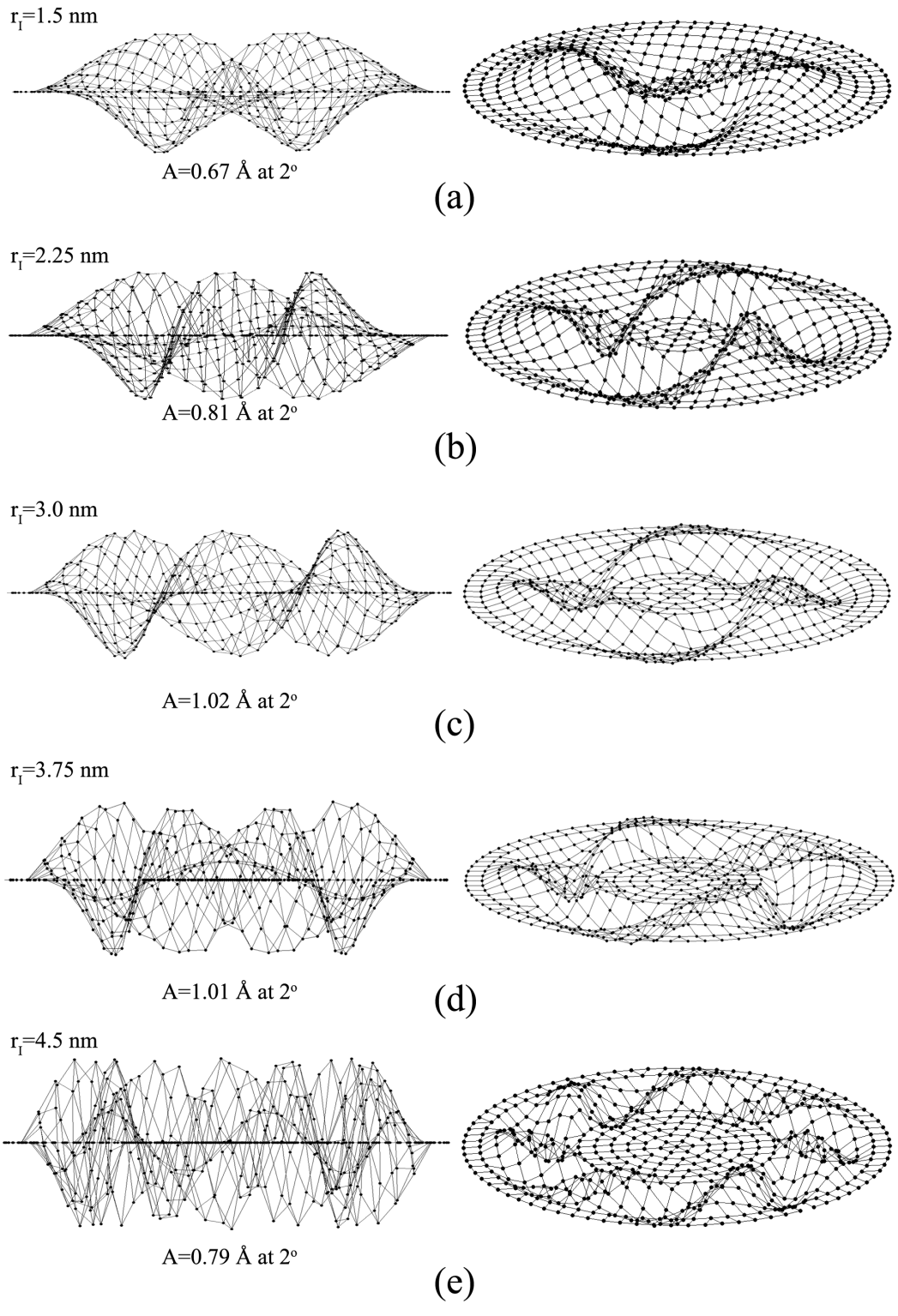

Fig. 13 Variation of wrinkle patterns for clamped circular graphene sheets (R_o = 9 nm).

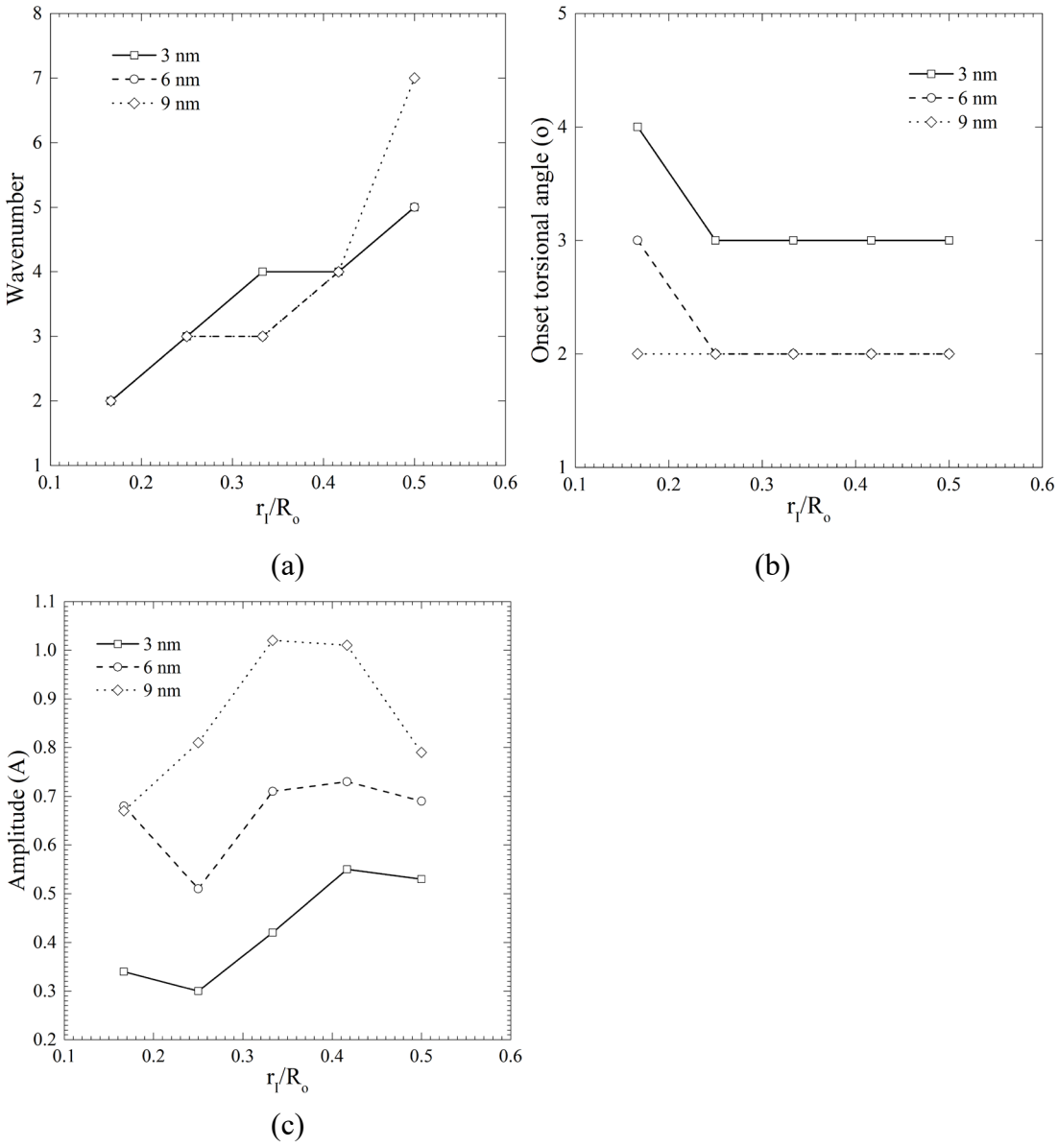

Fig. 14 Effects of wavenumber, wrinkle formation onset torsional angle and amplitude for circular graphene sheets with R_o=3, 6 and 9 nm.

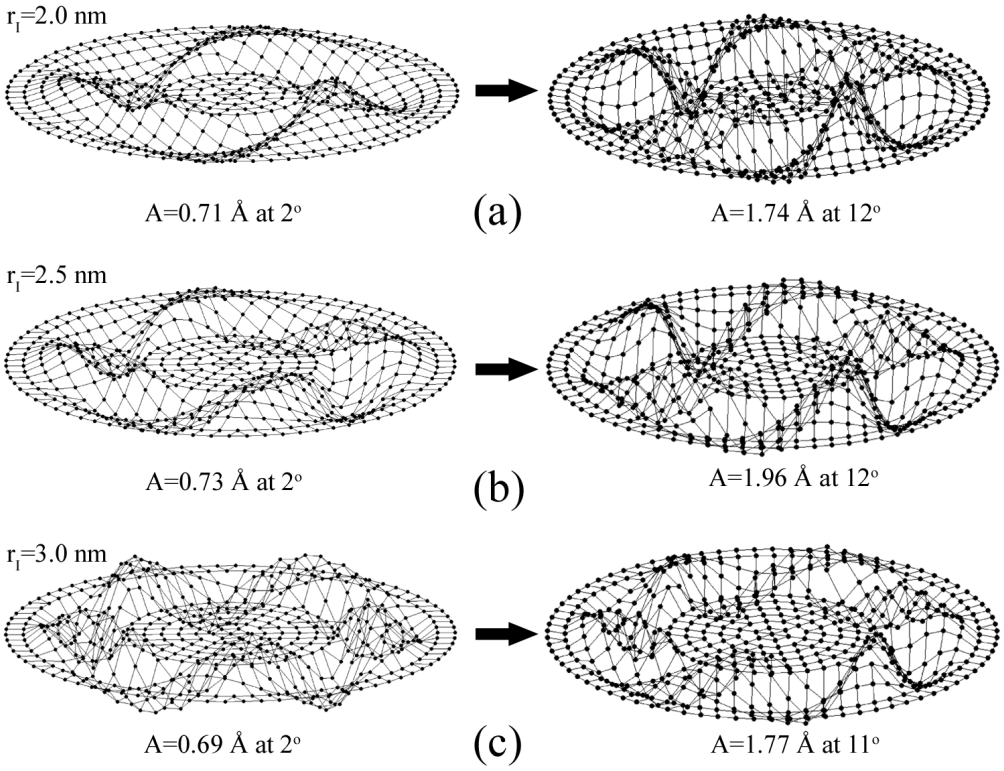

Fig. 15 Variation of wrinkle patterns for radial graphene sheets (R_o = 6 nm).

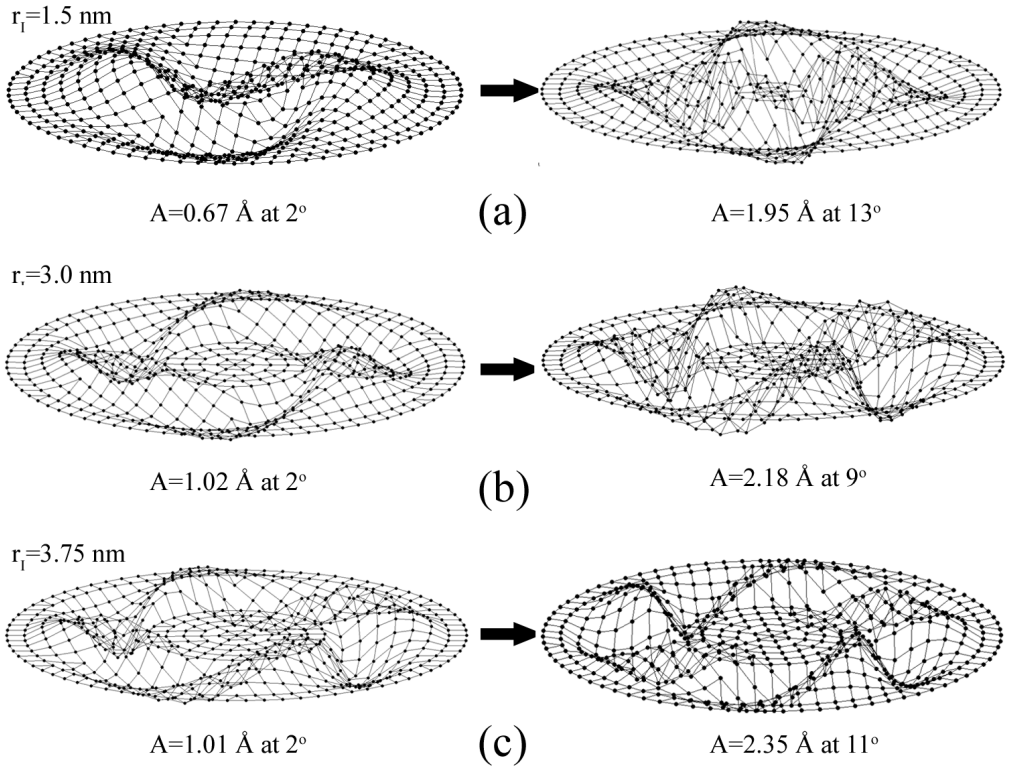

Fig. 16 Variation of wrinkle patterns for radial graphene sheets (R_o = 9 nm).